Atmos. Chem. Phys. Discuss., 11, 9375–9405, 2011
www.atmos-chem-phys-discuss.net/11/9375/2011/
doi:10.5194/acpd-11-9375-2011

Atmospheric Chemistry and Physics Discussions

Global precipitation response to changing external forcings since 1870

A. Bichet, M. Wild, D. Folini, and C. Schär

Institute for Atmospheric and Climate Sciences, ETH Zürich, Switzerland

Received: 5 January 2011 – Accepted: 10 March 2011 – Published: 22 March 2011

Correspondence to: A. Bichet (adeline.bichet@env.ethz.ch)

Published by Copernicus Publications on behalf of the European Geosciences Union.

Abstract

Predicting and adapting to changes in the hydrological cycle is one of the major challenges for the twenty-first century. To better estimate how it will respond to future changes in climate forcings, it is crucial to understand how it has evolved in the past and why. In our study, we use an atmospheric global climate model with prescribed sea surface temperatures (SSTs) to investigate how changing external climate forcings have affected global land temperature and precipitation in the period 1870–2005. We show that prescribed SSTs (encapsulating other forcings) are the dominant forcing driving the decadal variability of land temperature and precipitation since 1870. On top of this SSTs forcing, we also find that the atmosphere-only response to increasing aerosol emissions is a reduction in global land temperature and precipitation by up to 0.4 °C and 30 mm year^{-1}, respectively, between about 1930 and 2000. Similarly, the atmosphere-only response to increasing greenhouse gas concentrations is an increase in global land temperature and precipitation by up to 0.25 °C and 10 mm year^{-1}, respectively, between about 1950 and 2000. Finally, our results also suggest that between about 1950 and 1970, increasing aerosol emissions had a larger impact on the hydrological cycle than increasing greenhouse gases concentrations.

1 Introduction

Global and regional variations in temperature and precipitation are key parameters affecting our economy and ecosystems. To better predict them, it is essential to understand how they have evolved in the past and why. The past 150 years mark the changeover from a climate system dominated by natural influences to one significantly affected by anthropogenic activities. It is therefore of primary interest to understand how these changes in climate forcings have influenced the temperature and precipitation variations during this time period. Many reconstructions for these two variables cover the past century at global land scale (e.g., Peterson and Vose et al., 1997;

ACPD
11, 9375–9405, 2011

Mitchell and Jones, 2005; Brohan et al., 2006). Using observations, previous studies (e.g., Allen and Ingram, 2002; Wild et al., 2008; Wild and Liepert, 2010) have pointed out the crucial role of the radiation balance in driving the hydrological cycle and in particular its sensitivity to aerosols. In fact, many studies (e.g., Ramanathan et al., 2001; Liepert et al., 2004; Wild et al., 2005) show that increasing aerosol concentrations in the atmosphere are expected to cool the Earth's surface and reduce precipitation. Modelling studies have also shown the crucial role of the oceans in driving the hydrological cycle (Mitchell, 1983), and found a strong coupling between sea surface temperature (SST) and global land temperature (e.g., Hoerling et al., 2008; Compo et al., 2009) as well as precipitation (e.g., Koster and Suarez, 1995). In addition, many authors (e.g., Trenberth, 1990; Boer, 1993; IPCC, 2007; Trenberth, 2010) found that increasing the greenhouse gas concentrations and the associated temperature increase, via the resulting increase in evaporation and the Clausius-Clapeyron effect, should increase precipitation. Finally, it has also been argued that the hydrological sensitivity is larger for solar forcing (e.g. aerosols) than for carbon dioxide (CO_2) (e.g., Allen and Ingram, 2002; Lambert et al., 2004).

More work is still needed to fully understand the hydrological cycle response to changing external forcings. In particular, whereas most studies have investigated the climate response to doubling concentrations of CO_2, or the instant effects of aerosols, only few have examined the transient climate response to time varying concentrations of pollutants. In our study, we use an atmospheric general circulation model (GCM) forced with prescribed SSTs to quantify the global land temperature and precipitation transient response to changes in external climate forcings, since 1870. Section 2 outlines the methodology, Sect. 3 describes the results, and Sects. 4 and 5, respectively, discusses and concludes the study.

ACPD
11, 9375–9405, 2011

2 Methodology

2.1 Model set up and experimental design

We perform climate simulations using the fifth generation of the atmospheric GCM ECHAM5 (Roeckner et al., 2003). The basic prognostic variables, vorticity, divergence, temperature and surface pressure, are represented by spherical harmonics with triangular truncation, in our case at wave number 42 (T42), which implies a horizontal grid spacing of approximately 2.8°. Non-linear processes and physical parameterisation are solved on a corresponding Gaussian grid. In the vertical, 19 hybrid sigma-pressure levels are used, with the uppermost level at 10 hPa (Roeckner et al., 2003). Since direct and indirect aerosol effects have been previously shown to significantly affect global temperature and precipitation (e.g., Ramanathan et al., 2001; Stier et al., 2006), we use a version of ECHAM5 that is coupled to a fully interactive aerosol module, the Hamburg Aerosol Model (HAM) (Stier et al., 2005). This module predicts the evolution of microphysically interacting internally and externally mixed aerosol populations. The major global aerosol categories sulphate, black carbon (BC), particulate organic matter (POM), sea salt and mineral dust are included (Stier et al., 2005). Aerosol mixing ratios are transported in ECHAM5-HAM on the Gaussian grid using the algorithm of Lin and Rood (1996).

In our study, we use ECHAM5-HAM at resolution T42 for the time period 1870–2005, and conduct a series of experiments driven by prescribed SSTs and accounting for different atmospheric forcings. The forcings used include the time varying monthly mean of the solar irradiance (Solanski and Krivova, 2003), time varying stratospheric optical depth due to aerosols from explosive volcanoes (Sato et al., 1993), and time varying annual mean of greenhouse gas concentrations taken from observations until 2000 and from the IPCC A1B scenario for 2001–2005 (CO_2, methane, nitrous oxide, ozone and chlorofluorocarbons). Aerosol emissions of sulphur dioxide (SO_2), BC and POM are taken from the Japanese National Institute for Environmental Sciences (NIES) (Roeckner et al., 2006; Stier et al., 2006; Nozawa et al., 2007), and include geographically

ACPD
11, 9375–9405, 2011

resolved time varying monthly mean emissions from wildfires, agricultural burning and domestic fuel-wood consumption, as well as time varying annual mean emissions from fossil fuel consumption. To reduce the source of uncertainty coming from atmosphere-ocean coupling, we force our model with monthly mean observed SSTs and sea-ice concentrations, using gridded data from Rayner et al. (2003). It has been assembled by the Hadley Centre for Climatic Prediction and Research, and consists of monthly observed sea ice and SSTs from 1871 to present. It covers the global sea surface at 1° resolution, and uses a two-stage reduced-space optimal interpolation procedure, followed by superposition of quality-improved gridded observations onto the reconstructions to restore local detail. SSTs near sea ice are estimated using statistical relationships between SST and sea ice concentration (Rayner et al., 2003).

Previously, Hagemann et al. (2006) have studied the impact of model resolution on the hydrological cycle with ECHAM5, for the time period 1978–1999. They used horizontal resolutions going from T21 to T106, vertical resolutions going from 19 to 31 atmospheric layers, and forced ECHAM5 with prescribed SSTs and sea-ice dataset specifically constructed for the AMIP experiments by the NOAA Climate Analysis Centre (Gates, 1992). They show that in ECHAM5, increasing the vertical resolution is more beneficial than increasing the horizontal resolution, due to the improved moisture transport.

We perform twenty-five transient experiments, listed in Table 1. All the experiments run from 1870 to present and use a spin-up time ranging from several months to several years. The twenty-five experiments are divided into four ensembles: Thirteen experiments correspond to the control runs (CTRL, "all forcings run"), for which all the forcings are time varying (e.g. solar irradiance, greenhouse gases, aerosols and SSTs). Four experiments are identical to CTRL except that aerosol emissions (anthropogenic and natural) are held constant (referred to as AEC), six experiments are identical to CTRL except that SSTs are held constant (referred to as SSTC), and three experiments are identical to CTRL except that both, SSTs and aerosol emissions (anthropogenic and natural) are held constant (referred to as AESSTC). Note that in AESSTC, the only

ACPD
11, 9375–9405, 2011

remaining forcings expected to affect the climate at decadal scale are the greenhouse gases. Therefore, AESSTC can be used to evaluate the greenhouse gases effects.

To suppress the "noise" from individual simulations and assess their natural variability, we calculate ensemble means and quantify their uncertainties via the computation of their standard deviation (assuming a normal distribution). We also carried out tests with different ensemble sizes (not shown), and use at least three members ensemble to estimate the ensemble spread. In addition, we do not separate the aerosols emitted by explosive volcanoes from other aerosols (e.g. anthropogenic) in our sensitivity experiments, since no significant differences were found, in the 11-years running mean anomalies of global land temperature and precipitation, between simulations including the explosive volcanic emissions and simulations excluding them (not shown). This lack of differentiation may come from the prescribed SSTs. Therefore, when we refer to aerosol emissions in the following, they always include anthropogenic and natural (including explosive volcanic) aerosols. Finally, the climatological SSTs used in SSTC and AESSTC are averaged over the time period 1870–1900, since no significant differences were found, in the 11-years running mean anomalies of global land temperature and precipitation, between simulations using these climatological SSTs (1870–1900) and simulations using warmer climatological SSTs (1960–1990).

2.2 Evolution of the main climate forcings since 1870

This section describes the evolution of the climate forcings applied in our study since 1870: Namely, these are the aerosol emissions, the greenhouse gas concentrations, and the SSTs. Figure 1a–c presents the global annual mean emissions of SO_2, BC and OC (from NIES), and Fig. 1d presents the stratospheric optical depth due to explosive volcanoes (Sato et al., 1993). In addition, Fig. 1e presents the 11-years running mean of observed seasonal global SST anomalies, relative to the 1870–2000 mean (Rayner et al., 2003), including the contribution of surface water located under the ice.

According to Fig. 1a–c, SO_2 from fossil fuel (Fig. 1a, red curve) and OC from wildfires (Fig. 1c, green curve) had the highest increase in emissions since 1870. Aerosol

ACPD
11, 9375–9405, 2011

emissions from fossil fuel (red curves) increased slowly from 1870 to 1910, stabilized until 1930, increased rapidly until 1990, and then stabilized. Emissions from biofuel (black curves) and wildfires (green curves), as well as greenhouse gas concentrations (not shown), increased slowly from 1870 to the 1950s, and more rapidly after the 1950s. Large volcanoes were very active between 1870 and 1920, as well as between 1960 and 2000, but almost absent between 1920 and 1960 (Fig. 1d). Finally, global SST anomalies, in all seasons, were relatively stable from 1870 to 1910, increased until 1940, stabilized until 1970, and increased again until the present (Fig. 1e).

Increasing atmospheric greenhouse gas concentrations increases the downwelling infrared radiation (e.g. IPCC, 2007), which increases the surface temperature and evaporation. In turn, this is expected to increase the atmospheric moisture content, and ultimately precipitation (e.g., Trenberth, 1990). Increasing the aerosol emissions, however, decreases the downwelling shortwave radiation (direct aerosol effect) (e.g., Ramanathan et al., 2001), which decreases the surface temperature and evaporation. Since globally, evaporation changes have to be balanced by precipitation changes, this is in turn expected to decrease precipitation (e.g., Ramanathan et al., 2001; Wild and Liepert, 2010). Note that increasing absorbing aerosol emissions can also stabilize the atmospheric stratification and thereby suppress clouds formation and precipitation (semi-direct aerosol effect). Aerosol particles can also combine with clouds and trigger more numerous but smaller cloud droplets. This increases the cloud albedo and the cloud life-time (indirect aerosol effects), and reduces the temperature, evaporation and precipitation (Ramanathan et al., 2001). In principle, all these processes and feedbacks are represented in the ECHAM5-HAM model used in this study.

2.3 Observational data

To make full use of our results, we validate our simulations against observed temperature and precipitation datasets that cover the globe since 1870. Because historic observational data are scarce over the oceans, we limit our analysis to the land.

ACPD
11, 9375–9405, 2011

Our primary data is temperature. At least four datasets cover the global land temperature since 1880 (e.g., Hansen et al., 2001; Smith and Reynolds, 2004), and one even starts in 1850 (Brohan et al., 2006). According to the IPCC fourth assessment report (2007), the global land annual means of these five datasets are in good agreement since 1880. Therefore, we validate our simulated temperatures against one single gridded temperature dataset, the "CRUTEM3", starting in 1850 (Brohan et al., 2006). It has been assembled by the Climate Research Unit of the University of East Anglia (CRU), and consists of monthly observed air temperatures from 1850 to present. It is based on 4349 stations, and covers the global land surface at 5° resolution. It uses an interpolation method such that each grid box value is the mean of all available station anomaly values, except that station outliers in excess of five standard deviations are omitted. In addition, it does not use infilling for the missing values, and most gaps are found in the tropics and in the Southern Hemisphere, particularly Antarctica. Gaps are also larger in the ninetieth century and during the two world wars (Brohan et al., 2006). Note that when comparing observed against simulated temperature, we change the grid of the simulated temperatures each year according to the data coverage.

We validate our simulated precipitation against two observational datasets starting in 1901. The first gridded precipitation dataset, "CRU TS 2.1" (Mitchell and Jones, 2005), has been assembled by the CRU, and consists of monthly observed precipitation for the period 1901–2002. It covers the global land surface at 0.5° resolution and includes oceanic islands but excludes Antarctica. The interpolation is done directly from station observations, and uses the angular distance-weighting method. Similar as with temperature, the station data values are first transformed into anomalies relative to a standard normal period prior to interpolation (New et al., 2001). This dataset has not been corrected for gauge biases, and this is expected to lead mostly to an undercatch of solid precipitation in colder areas (New et al., 2000).

The second gridded precipitation dataset, "Global Historical Climate Network" (GHCN) (Peterson and Vose, 1997), has been assembled by the National Oceanic and Atmospheric Administration, and consists of monthly observed precipitation calculated

ACPD
11, 9375–9405, 2011

from the GHCN V2 dataset, for the period from 1900 to 2009. It covers the global land surface at 5° resolution, and is the most comprehensive dataset of monthly precipitation covering the entire twentieth century. It comprises stations with varying temporal coverage, going from 5500 in 1900 to 16 500 in 1966 (New et al., 2001).

While both datasets, CRU and GHCN, are reconstructed from gauge only measurements, only the CRU dataset is spatially infilled by interpolation (IPCC, 2007). Note also that although gauge measurements offer great temporal coverage, their main limitation comes from their poor spatial coverage in many parts of the world, particularly in the high latitudes, arid regions, and parts of the tropics (New et al., 2001). Finally, even though no quantified uncertainties are given with these observational datasets, one should keep in mind that gauge measurements are subject to errors, biases and inhomogeneity arising from several sources (New et al., 2000, 2001).

3 Results

This section describes our main results: Sect. 3.1 evaluates the capacity of ECHAM5-HAM to reproduce the observations, and Sect. 3.2 presents the sensitivity experiments. All the time series are shown as 11-years running mean anomalies, and the reference periods vary according to the analysis. We first calculate the anomalies, then the global means, and finally the 11-years running means.

3.1 Global scale assessment of the model

This section compares the ensemble mean from CTRL with observations. The global land temperature anomalies, relative to the 1960–1990 mean, are shown as 11-years running mean in Fig. 2. Note that in the model, temperatures correspond to surface temperatures, not two meters temperatures. Qualitatively, the temperature anomalies from CTRL (solid line) are in good agreement with observations (dashed line) since 1870, particularly in the June-July-August (JJA) and September-October-November

ACPD
11, 9375–9405, 2011

(SON) averages (Fig. 2). In agreement with the annual means from the IPCC fourth assessment report (2007), simulated (CTRL) and observed global land annual temperature anomalies show two warming periods of about 0.5 °C each: one from 1910 to 1940, and a second one after 1980. According to Fig. 2, this is the case in all seasons. However, two periods with warm biases occur in the annual averages: One in the late ninetieth century (0.2 °C on average), and one in the 1940s and 1950s (0.1 °C on average), both particularly pronounced in the December-January-February (DJF) and March-April-May (MAM) averages. Regarding the first warm bias in the late ninetieth century, Fig. 3 shows that it is present over most of the land surfaces but most pronounced in Siberia. Note that interior of continents such as Siberia are least constrained by SSTs in the model, and therefore have likely larger biases. Regarding the second warm bias in the 1940s and 1950s, it falls into a period with a general underestimation of SSTs due to changes in observational practice (Thompson et al., 2008). However, this cold bias in driving SSTs should imply a cold simulated bias in land temperatures, opposite to the model results. Thus the bias in the second period might actually be somewhat larger than indicated in Fig. 3.

The global land precipitation anomalies, relative to the 1901–2000 mean, are shown as 11-years running mean in Fig. 4. Qualitatively, the precipitation anomalies from CTRL (solid line) are in a reasonable agreement with observations (dashed line) since 1901, particularly in JJA and SON (Fig. 4), although the decadal variations are significantly underestimated. In agreement with the annual means from New et al. (2001) and from the IPCC fourth assessment report (2007), simulated (CTRL) and observed global land annual precipitation anomalies show an increase of about 30 mm year^{-1} from 1901 to the 1950s, a decline until the early 1990s, and then a recovery. However, whereas the observed anomalies increase overall by about 10 mm year^{-1} from 1901 to present, the simulated anomalies (CTRL) decrease by about the same amount during this time period. Note however that these century trends are relatively small compared with the inter-annual and multi-decadal variability.

ACPD
11, 9375–9405, 2011

A wet bias occurs in the annual averages in the 1920s and 1930s, particularly pronounced in JJA and DJF (Fig. 4), and mostly located in the tropics (e.g. the Amazon region, China and Indonesia) (Fig. 5). According to New et al. (2001), the tropical regions are poorly covered by observations prior to 1950s. In addition, the tropics are the region with highest precipitation and highest latitudinal weighting at global scale, which leads to a global precipitation signal dominated by the precipitation between 20° S and 20° N. Therefore, we conclude that the global mean wet bias in the 1920s and 1930s can be ascribed to a large degree to tropical regions, and may partly be ascribed to inaccuracies in the observational data. In addition, the 1930s wet bias located in North America in JJA and MAM (Fig. 5) could be related to the "dust bowl" event: In the 1930s, the low precipitation observed in North America has been argued to be worsened by the land-use change in the Great Plains (e.g., Cook et al., 2009; Findell et al., 2009). Since the land-use change is not included in our experiments, we can expect that our model does not simulate the positive feedback leading to further precipitation decrease. Finally, the observations include a complex response to tropical SST anomalies and to ENSO (Brönniman et al., 2007), which is likely not fully captured by the model.

3.2 Global scale sensitivity of the model to external forcing

In this section, we compare the ensemble means from the different sensitivity studies. Figure 6 shows the global land temperature anomalies, relative to the 1870–1880 mean, shown as 11-years running means. The different experiments presented in Fig. 6 are the ensemble means from CTRL (black curve), SSTC (blue curve), AEC (red curve), and AESSTC (green curve) (see Table 1 and Sect. 2.1). To begin the discussion, we note that the different ensembles corresponding to these forcings significantly depart from each other. In addition, since the annual land temperature anomalies resemble the seasonal anomalies at least qualitatively (Fig. 6), we focus our discussion on annual means only. According to Fig. 6, the global land temperature anomalies simulated in CTRL (black curve) show a large decadal variability since 1870, that is

ACPD
11, 9375–9405, 2011

suppressed in experiments with climatological SSTs, namely SSTC (blue curve) and AESSTC (green curve): Not present in the SSTC simulations, are, in particular, the two temperature increases from 1910 to 1940 and 1980 to 2000. Instead, the anomalies simulated in SSTC are constant until 1950, decrease by about 0.2 °C from 1950 to 1990, and then recover. On the other hand, the anomalies simulated in AESSTC (green curve) are constant until about 1950, and then increase by about 0.25 °C from 1950 to 2000. Finally, the anomalies simulated in AEC (red curve) show a decadal variability similar to the one simulated in CTRL (black curve) since 1870, but exhibit a larger trend after about 1930 (up to 0.4 °C warmer in 2000).

Figure 7 shows the global land precipitation anomalies, relative to the 1870–1880 mean, shown as 11-years running means. For the same reasons as in the case of temperature, we focus our discussion on annual means only. According to Fig. 7, the global land precipitation anomalies simulated in CTRL (black curve) show large decadal variations since 1870, that is suppressed in experiments with climatological SSTs, namely SSTC (blue curve) and AESSTC (green curve): Not present in the SSTC simulations are, in particular, the two precipitation maxima in the late 1930s and the late 1950s. Instead, the anomalies simulated in SSTC are constant until 1930, smaller by about 20 mm year^{-1} between 1930 and 1970, and then stabilize. On the other hand, the anomalies simulated in AESSTC (green curve) are constant until about 1930, and increase by about 10 mm year^{-1} from 1930 to 2000. Finally, the anomalies simulated in AEC (red curve) show decadal variations similar to the one simulated in CTRL (black curve), but exhibit a larger trend after about 1930 (up to 30 mm year^{-1} in 2000). This even leads to a change of the global land precipitation centennial trend sign from positive (without aerosols, red curve) to negative (with aerosols, black curve). Note that even though the representation of aerosol variations with HAM overall improves the agreement with observations, it appears that aerosol effects might have been overestimated in our simulations, leading to a too large effect on the climate (Figs. 4 and 7).

ACPD
11, 9375–9405, 2011

4 Discussion

In the previous section, we showed that changing external forcings have significantly affected the global land temperature and precipitation since 1870. The next sections examine the physical processes behind these sensitivities. We focus our discussion on precipitation.

4.1 Origin of water in global land precipitation

At global scale, the water that precipitates over land has two sources: the land evaporation and the advection of oceanic moisture. In the CTRL experiments, the global land evaporation is about 500 mm year^{-1} (Fig. 8a, black curve), whereas the global land precipitation is about 760 mm year^{-1} (not shown). Thereby, in agreement with previous studies (e.g., Wild et al., 2008), we find that at least 35% (260 mm year^{-1}) of global land precipitation must come from oceanic evaporation (Fig. 8b, black curve). In addition, our results suggest that the global land precipitation trend (−0.92 mm decade^{-1}, Fig. 7, black curve) and variability, since 1870, primarily respond to the trend and variability of the global land evaporation (−0.77 mm decade^{-1} and $r^2 = 0.81$, respectively, Fig. 8a, black curve), rather than global oceanic evaporation (−0.15 mm decade^{-1} and $r^2 = 0.36$, respectively, not shown).

The next sections investigate the sensitivity of the global land and oceanic evaporation to changing external forcings since 1870.

4.2 Control of evaporation in our experiments

In this section, we discuss simulated changes in evaporation over sea and land. Over sea, evaporation is directly driven by the prescribed SSTs in our modelling framework. Over land, potential evaporation is according to the Penman equation driven by the surface energy balance (primarily governed by the net surface radiation balance) and by the moisture holding capacity of the air (governed by the Clausius-Clapeyron relation)

ACPD
11, 9375–9405, 2011

(e.g., Penman, 1950; Hartmann, 1994). Changes in land evapotranspiration will in addition depend upon changes in the availability of water (soil moisture).

Over the oceans, where moisture is unlimited, the net surface radiation is mostly transferred into latent heat (Bowen ratio from CTRL = 0.14, not shown). Over land, where evaporation may be soil moisture limited, the net surface radiation is more equally distributed between latent and sensible heat (Bowen ratio from CTRL = 0.85, Fig. 8c, black curve). In the CTRL experiments, in terms of 11-years running mean variability, the global land net surface radiation (Fig. 8d, black curve) explains 76% of the global land latent heat flux (Fig. 8a, black curve, $r^2 = 0.76$). This suggests that the remaining 24% are explained by changes in soil moisture, and/or changes in the moisture holding capacity of the air, both being influenced by changing properties of the air advected from the oceans. About 0.8 W m^{-2} of land latent heat is needed to evaporate 10 mm year^{-1} (Fig. 8a).

Finally, our experimental set up (prescribed SSTs) implies that in our simulations, the oceanic heat fluxes are not limited by the net surface radiation as in reality. In particular, the ocean is not able to respond to the changes in external forcings applied in the sensitivity experiments. Therefore, our sensitivity experiments assess the atmosphere-only response to changes in external forcing, and do not take into account the eventual changes happening over the oceans. The next sections first investigate, since 1870, the SSTs impact on the global land temperature and precipitation, and then, the atmosphere-only response of the climate system to changing climate forcings.

4.3 Role of SSTs

In this section, we compare the ensemble means from CTRL (black curve) and SSTC (blue curve), which differ from each other only by their prescribed SSTs. Note that the discussion is equally valid for the comparison between the ensemble means from AEC (red curve) and AESSTC (green curve). Figures 6 and 7 show that SSTs affect the decadal variability of the global land temperature and precipitation: compared with fully

ACPD
11, 9375–9405, 2011

transient simulations, simulations with climatological SSTs show hardly any decadal variability in these variables. The high correlation coefficient between the global annually averaged time series of SSTs and land temperature from CTRL ($r^2 = 0.85$), indicates in line with previous studies (e.g., Hoerling et al., 2008; Compo and Sardeshmukh, 2009; Findell et al., 2009) that the two variables are strongly coupled. According to Compo and Sardeshmukh (2009), warmer SSTs increase land temperatures primarily via moistening and warming of the air over land, which then increases the downward longwave radiation at the surface.

In our experiments, between 1920 and 1980, warmer transient SSTs (CTRL, black curves), as compared to 1871–1900 climatological SSTs (SSTC, blue curve), increase the global land P-E (Fig. 8b) (equivalent to the net advection of moisture from ocean to land), as well as the moisture holding capacity of the air over land. Thereby, this warmer, moister air coming from the ocean increases the global land temperature (Fig. 6), precipitation (Fig. 7), soil moisture (Fig. 8e) and evaporation (Fig. 8a), and decreases the global land Bowen ratio (Fig. 8c). Land evaporation may here change due to a moistening of the soil (Fig. 8e), changes in net surface radiation (Fig. 8d), and/or due to the warming (Fig. 6) and associated increase in air capacity. About two third of the global land precipitation increase is in the form of convective precipitation (Fig. 8f,g), mostly located in the tropics (Fig. 9a). After about 1980, warmer transient SSTs, as compared to climatological SSTs, no longer enhance the net advection of moisture from the oceans (Fig. 8b), which indicates a weakening of the atmospheric circulation and associated moisture transport and/or a weakening of precipitation formation (e.g. through changes in convection activity and/or atmospheric stability). Thereby, over land, the global precipitation (Fig. 7), soil moisture (Fig. 8e), and evaporation (Fig. 8a) no longer increase, and the global land Bowen ratio no longer decreases (Fig. 8c).

ACPD
11, 9375–9405, 2011

4.4 Role of aerosols and greenhouse gases

We first compare the ensemble means from CTRL (black curves) and AEC (red curves), which differ from each other only by their aerosol emissions. Figures 6 and 7 show that after about 1930, increasing aerosol emissions decreases the global land temperature and precipitation by up to 0.4 °C and 30 mm year^{-1}, respectively. Meanwhile, the decadal variability remains essentially unaffected. Our results support at least three mechanisms responsible for this precipitation decrease: less land surface radiation, less transport from the oceans and potentially stronger stability of the atmosphere. According to Fig. 8h, at global land scale, increases in aerosol radiative forcing decrease the net surface solar radiation after about 1930 by up to 6.2 W m^{-2}. This decreases the net surface radiation by up to 5.4 W m^{-2} (Fig. 8d) and the latent heat flux by up to 2 W m^{-2} (equivalent to about 23 mm year^{-1} in evaporation, Fig. 8a). Finally, about two third of the global land precipitation decrease is in the form of convective precipitation (Fig. 8f,g), mostly located in the tropics (Fig. 9b). Especially absorbing aerosols can reduce convection by increasing the atmosphere stability (semi-direct aerosol feedback), as they cool the surface on the one hand (Fig. 6) and warm the troposphere on the other hand (in layers containing the absorbing aerosols). Decrease in convection will implicitly also decrease the net advection of moisture from the oceans, which is consistent with the results (Fig. 8b).

We now look at the AESSC ensemble mean (green curves), which corresponds to the simulations where greenhouse gases constitute the only transient forcing. Figures 6 and 7 show that the atmospheric response to increasing greenhouse gas concentrations after about 1950 results in increasing the global land temperature and precipitation by up to 0.25 °C and 10 mm year^{-1}, respectively. Note that this increase is found despite the unchanged SSTs in our experimental set up. At global land scale, the greenhouse gases radiative properties increase the net surface radiation by up to 1 W m^{-2} (Fig. 8d) and the latent heat flux by up to 0.4 W m^{-2} (equivalent to about 5 mm year^{-1} of evaporation) (Fig. 8a), after about 1950. In addition, increasing

ACPD
11, 9375–9405, 2011

greenhouse gas concentrations also increases the amount of moisture advected from the oceans (Fig. 8b).

The combined effect of aerosols and greenhouse gases is apparent in the SSTC (blue curve) ensemble mean. In agreement with previous studies (e.g., Wild et al., 2007; Liepert and Wild, 2010), our results suggest that between about 1950 and 1970, the atmosphere-only aerosol effect is dominant, as temperature and precipitation both decrease. Later on, greenhouse gases start to dominate again, and there is no further decrease in either temperature or precipitation, despite further increase of aerosol emission between 1970 and 1990 (Fig. 1a–c).

Finally, note that in our experiments, transient aerosol emissions (CTRL), as compared to constant aerosol emissions (AEC), decrease the global oceanic net surface radiation by up to 3 $W\,m^{-2}$, since 1870 (not shown). In reality, this is expected to cool the SSTs and further decrease the global land temperature and precipitation (Sect. 4.3). However, this cannot be the case with our experimental set up (prescribed SSTs). Therefore, we suggest that the full system response (including the ocean feedback) to increasing aerosol emissions, should be larger than the response of the atmosphere-only response discussed in our study. Similarly, we expect the full system response to increasing greenhouse gas concentrations, to be larger than the atmosphere-only response discussed in our study.

5 Conclusions

We have shown that with prescribed SSTs, despite using a relative coarse resolution, ECHAM5-HAM satisfactorily reproduces the observed global land temperature and precipitation anomalies, since 1870 and 1901, respectively. The sensitivity studies suggest that in our framework, SSTs (encapsulating other forcings) are a dominant forcing, driving trends and decadal variations of global land temperature and precipitation since 1870. In addition, we showed that the atmosphere-only response to increasing aerosol emissions after 1930 amounts to a decrease in global land temperature and

ACPD
11, 9375–9405, 2011

precipitation by up to 0.4 °C and 30 mm year^{-1}, respectively. Similarly, the atmosphere-only response to increasing greenhouse gas concentrations results in an increase in global land temperature and precipitation by up to 0.25 °C and 10 mm year^{-1}, respectively, after about 1950. Finally, in agreement with previous studies (e.g., Wild et al., 2007, 2008; Liepert and Wild, 2010), we suggest that between about 1950 and 1970, the aerosols impact on global land temperature and precipitation is larger than the greenhouse gases impact, whereas the opposite is true after 1970, partly due to the stabilization of aerosol emissions after about 1990.

Acknowledgement. The authors thank the MPI Hamburg for providing access to the ECHAM5-HAM code and colleagues at ETH Zürich who contributed to model development, in particular Ulrike Lohmann. This research has partly been supported by the NCCR Climate funded by the Swiss National Science Foundation. The simulations were done on the CRAY XT-5 at the Swiss National Supercomputing Centre (CSCS) in Manno, Switzerland.

References

Allen, M. R. and Ingram, W. J.: Constraints on future changes in climate and the hydrological cycle, Nature, 419, 224–232, 2002.

Boer, G. J.: Climate change and the regulation of the surface moisture and energy budgets, Clim. Dynam., 8, 225–239, 1993.

Brohan, P., Kennedy, J. J., Harris, I., Tett, S. F. B., and Jones, P. D.: Uncertainty estimates in regional and global observed temperature changes: a new data set from 1850, J. Geophys. Res., 111, 12106, doi:10.1029/2005JD006548, 2006.

Brönniman, S., Xoplaki, E., Casty, C., Pauling, A., and Luterbacher, J.: ENSO influence on Europe during the last centuries, Clim. Dynam., 28, 181–192, 2007.

Cook, B. I., Miller, R. L., and Seager, R.: Amplification of the North American "Dust Bowl" drought through human-induced land degradation, P. Natl. Acad. Sci. USA, 106, 4997–5001, 2009.

Compo, G. P. and Sardeshmukh, P. D.: Oceanic influences on recent continental warming, Clim. Dynam., 32, 333–342, 2009.

ACPD
11, 9375–9405, 2011

Findell, K. L., Pitman, A. J., England, M. H., and Pegion, P. J.: Regional and global impacts of land-cover changes and sea-surface temperature anomalies, J. Climate, 22, 3248–3269, 2009.
Gates, W. L.: AMIP: The Atmospheric Model Intercomparison Project, B. Am. Meteor. Soc., 73, 1962–1970, 1992.
Hagemann, S., Arpe, K., and Roeckner, E.: Evaluation of the hydrological cycle in the ECHAM5 model, J. Climate, 19, 3810–3827, 2006.
Hansen, J., Ruedy, R., Sato, M., Imhoff, M. L., Lawrence, W. T., Easterling, D. R., Peterson, T. C., and Karl, T. R.: A closer look at United States and global surface temperature change, J. Geophys. Res., 106, 23947–23963, 2001.
Hartmann, D. L.: Global Physical Climatology, International Geophysics Series, 56, edited by: Smowska, R. and Holton, J. R., Academic Press Limited, London, 1994.
Hoerling, M., Kumar, A., Eischeid, J., and Jha, B.: What is causing the variability in global mean land temperature?, Geophys. Res. Lett., 35, 23712, doi:10.1029/2008GL035984, 2008.
ICCP: Contribution of Working Group I to the Fourth Assessment Report of the Intergovernmental Panel on Climate Change, edited by: Solomon, S., Qin, D., Manning, M., Chen, Z., Marquis, M., Averyt, K. B., Tignor, M., and Miller H. L., Cambridge University Press, Cambridge, 2007.
Koster, R. D. and Suarez, M. J.: Relative contributions of land and ocean processes to precipitation variability, J. Geophys. Res., 100, 13775–13790, 1995.
Lambert, F. H., Scott, P. A., Allen, M. R., and Palmer, M. A.: Detection and attribution of changes in 20th century land precipitation, Geophys. Res. Lett., 31, 10203, doi:10.1029/2004GL019545, 2004.
Liepert, B. G., Feichter, J., Lohmann, U., and Roeckner, E.: Can aerosols spin down the water cycle in a warmer and moisture world?, Geophys. Res. Lett., 31, 06207, doi:10.1029/2003GL019060, 2004.
Lin, S. J. and Rood, R. B.: Multidimentional flux-form semi-Lagrangian transport scheme, Mon. Weather Rev., 124, 2046, doi:10.1175/1520-0493, 1996.
Mitchell, J. F. B.: The seasonal response of a general circulation model to change in CO_2 and sea temperatures, Quaternary J. Res. Meteorol. Soc., 109, 113–152, 1983.
Mitchell, J. F. B., Wilson, C. A., and Cunnington, W. M.: On CO_2 climate sensitivity and model dependence of results, Quaternary J. Res. Meteorol. Soc., 113, 293–322, 1987.
Mitchell, T. D. and Jones, P. D.: An improved method of constructing a database of monthly

ACPD
11, 9375–9405, 2011

climate observations and associated high resolution grids, Int. J. Climatol., 25, 693–712, 2005.
New, M., Hulme, M., and Jones, P. D.: Representing twentieth-century space–time climate variability. Part II: Development of 1901–96 monthly grids of terrestrial surface climate, J. Climate, 13, 2217–2238, 2000.
New, M., Todd, M., Hulme, M., and Jones, P. D.: Precipitation measurements and trends in the twentieth century, Int. J. Climatol., 21, 1899–1922, 2001.
Nozawa, T., Nagashima, T., Ogura, T., Yokohata, T., Okada, N., and Shiogama, H.: Climate change simulations with a coupled ocean-atmosphere GCM called the model for interdisciplinary research on climate: MIROC. CGER's Tech. Rep., Natl. Inst. For Environ. Stud., Japan, http://www.cger.nies.go.jp/publications/report/i073/I073.pdf, 2007.
Penman, H. L.: The dependence of transpiration on weather and soil conditions, J. Soil. Sci., 1, 74–89, 1950.
Peterson, T. C. and Vose, R. S.: An overview of the global historical climatology network temperature database, B. Am. Meteorol. Soc., 78, 2837–2849, 1997.
Ramanathan, V., Crutzen, P. J., Kiehl, J. T., and Rosenfeld, D.: Aerosols, climate, and the hydrological cycle, Science, 294, 2119–2124, 2001.
Rayner, N. A., Parker, D. E., Horton, E. B., Folland, C. K., Alexander, L. V., Rowell, D. P., Kent, E. C., and Kaplan, A.: Global analyses of sea surface temperature, sea ice, and night marine air temperature since the late nineteenth century, J. Geophys. Res., 108, 4407, doi:10.1029/2002JD002670, 2003.
Roeckner, E., Baeuml, G., Bonventura, L., Brokopf, R., Esch, M., Giorgetta, M., Hagemann, S., Kirchner, I., Kornblueh, L., Manzini, E., Rhodin, A., Schlese, U., Schulzweida, U., and Tompkins, A.: The atmospheric general circulation model ECHAM5. PART I: Model description, Report 349, Max-Planck-Institute for Meteorology, 2003.
Roeckner, E., Stier, P., Feichter, J., Kloster, S., Esch, M., and Fischer-Bruns, I.: Impact of carbonaceous aerosol emissions on regional climate change, Clim. Dynam., 27, 553–571, 2006.
Sato, M., Hansen, J. E., McCormick, M. P., and Pollack, J. B.: Stratospheric aerosol optical depths, 1850–1990, J. Geophys. Res., 98, 22987–22994, 1993.
Smith, T. M. and Reynolds, R. W.: Improved extended reconstruction of SST (1854–1997), J. Climate, 17, 2466–2477, 2004.
Solanki, S. K. and Krivova, N. A.: Can solar variability explain global warming since 1970?, J.

ACPD
11, 9375–9405, 2011

Geophys. Res., 108, 1200, doi:10.1029/2002JA009753, 2003.
Stier, P., Feichter, J., Kinne, S., Kloster, S., Vignati, E., Wilson, J., Ganzeveld, L., Tegen, I., Werner, M., Balkanski, Y., Schulz, M., Boucher, O., Minikin, A., and Petzold, A.: The aerosol-climate model ECHAM5-HAM, Atmos. Chem. Phys., 5, 1125–1156, doi:10.5194/acp-5-1125-2005, 2005.
Stier, P., Feichter, J., Roeckner, E., Kloster, S., and Esch, M.: The evolution of the global aerosol system in a transient climate simulation from 1860 to 2100, Atmos. Chem. Phys., 6, 3059–3076, doi:10.5194/acp-6-3059-2006, 2006.
Thompson, D. W. J., Kennedy, J. J., Wallace, J. M., and Jones, P. D.: A large discontinuity in the mid-twentieth century in observed global-mean surface temperature, Nature, 453, 646–649, 2008.
Trenberth, K. E.: Conceptual framework for changes of extremes of the hydrological cycle with climate change, Climatic Change, 42, 327–339, 1990.
Trenberth, K. E.: Changes in precipitation with climate change, Clim. Res., in press, doi:10.3354/cr00953, 2011.
Wild, M. and Liepert, B. G.: The Earth radiation balance as driver of the global hydrological cycle, Environ. Res. Lett., 5, 025203, doi:10.1088/1748-9326/5/2/025203, 2010.
Wild, M., Gilgen, H., Roesch, A., Ohmura, A., Long, C. N., Dutton, E. G., Forgan, B., Kallis, A., Russak, V., and Tsvetkov, A.: From dimming to brightening: decadal changes in solar radiation at Earth's surface, Science, 308, 847–850, 2005.
Wild, M., Ohmura, A., and Makowski, K.: Impact of global dimming and brightening on global warming, Geophys. Res. Lett., 34, 04702, doi:10.1029/2006GL028031, 2007.
Wild, M., Grieser, J., and Schär, C.: Combined surface solar brightening and increasing greenhouse effect support recent intensification of the global land-based hydrological cycle, Geophys. Res. Lett., 35, 17706, doi:10.1029/2008GL034842, 2008.

ACPD
11, 9375–9405, 2011

Global precipitation response to changing external forcings since 1870

A. Bichet et al.

Table 1. Summary of the different simulations. All the simulations cover the period 1870 to 2005 and are forced with time-varying greenhouse gas concentrations since 1870.

Name of ensemble mean	Number of experiments	SSTs	Aerosol emissions
CTRL	13	Time-varying since 1870	Time-varying since 1870
AEC	4	Time-varying since 1870	Constant to 1870 value
SSTC	6	Climatology averaged over 1871–1900	Time-varying since 1870
AESSTC	3	Climatology averaged over 1871–1900	Constant to 1870 value

ACPD
11, 9375–9405, 2011

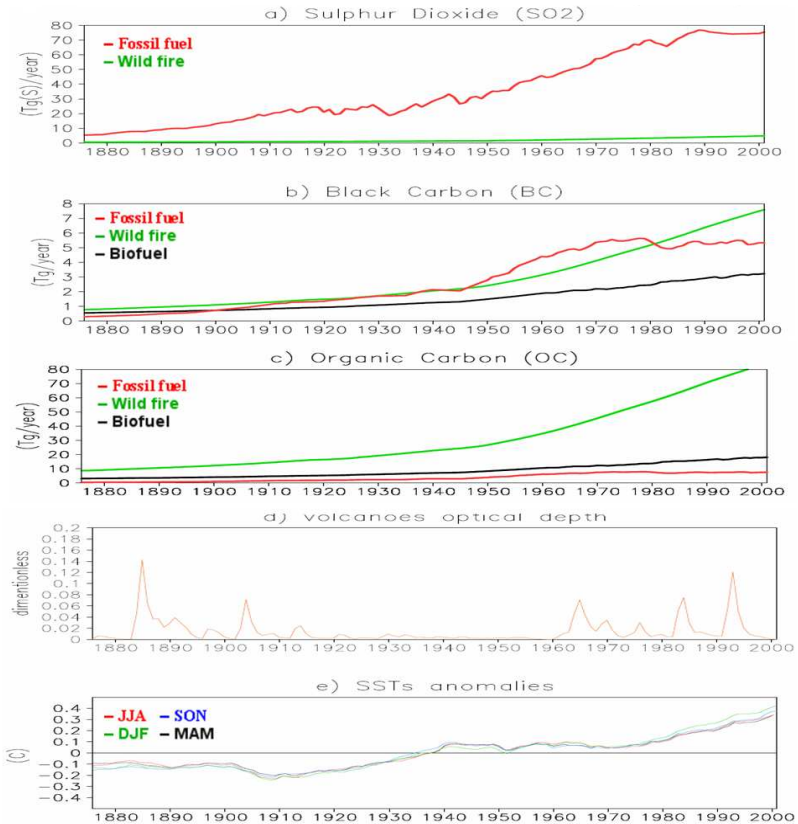

Fig. 1. Global annual time series of anthropogenic aerosol emissions **(a–c)** and stratospheric optical depth due to explosive volcanoes **(d)**, and global seasonal time series of SST anomalies shown as 11-years running means **(e)**. The SST anomalies are in °C, and correspond to the SST global mean value for each year, minus the global mean of the reference period (1870–2000).

ACPD
11, 9375–9405, 2011

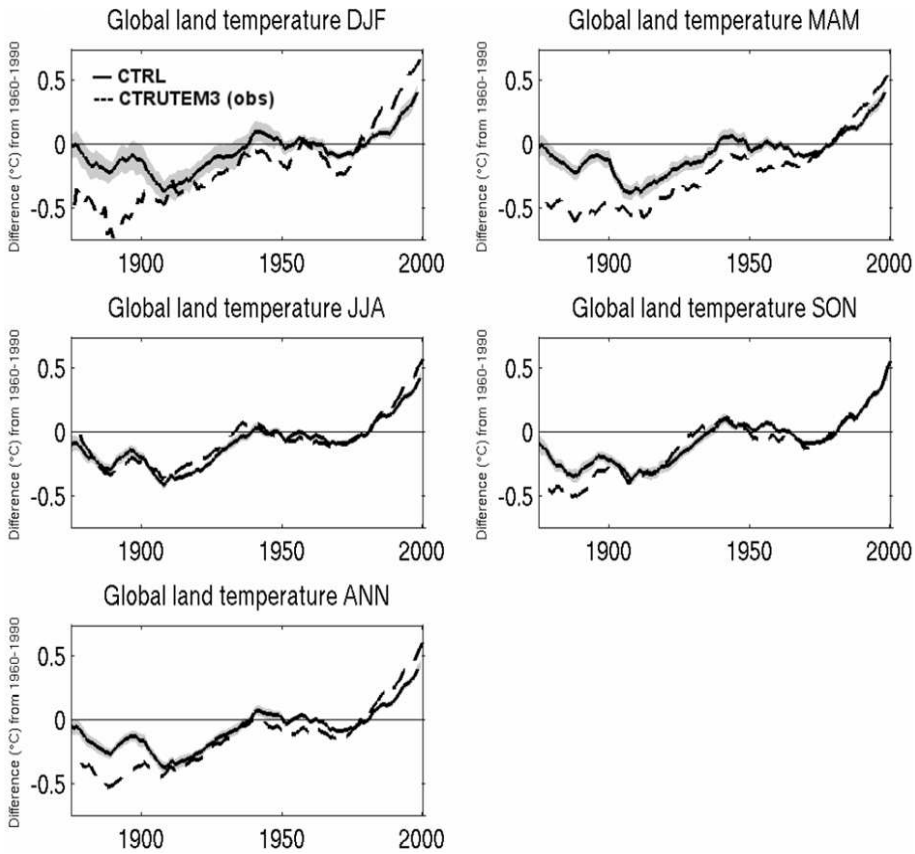

Fig. 2. Simulated (CTRL, solid) and observed (CRUTEM3, dashed) annual and seasonal global land temperature anomalies (°C), relative to the 1960–1990 mean, shown as 11-years running means. Gray shaded area corresponds to the ±1 sigma spread of the ensemble CTRL.

ACPD
11, 9375–9405, 2011

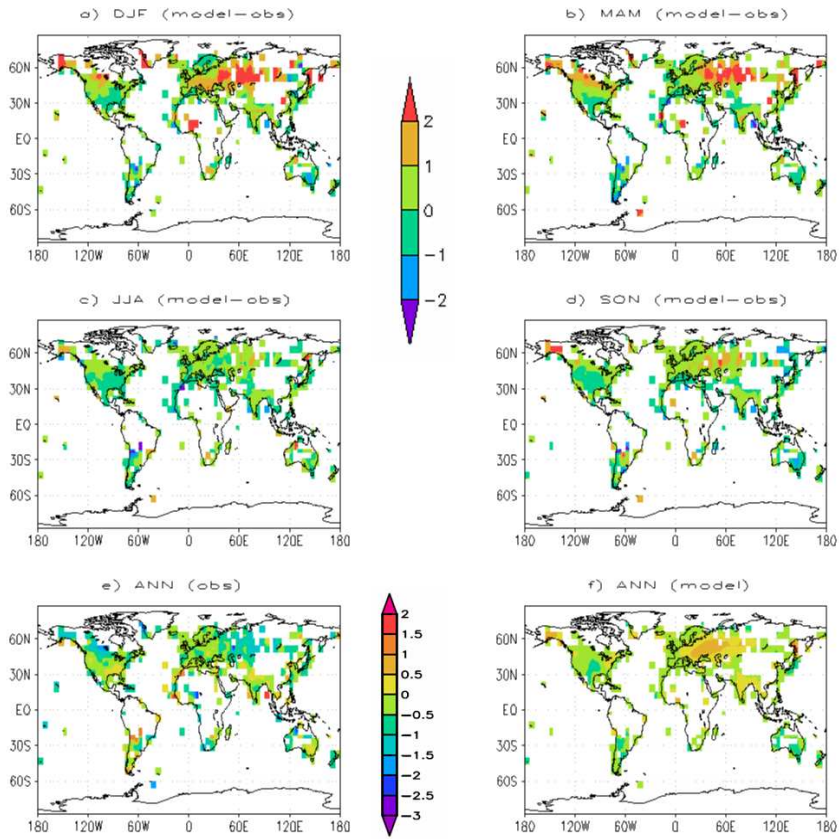

Fig. 3. Maps of seasonal land temperature biases (°C) averaged over the time period 1890–1900 **(a–d)**. The biases maps correspond to the difference between the temperature anomalies (ref = 1960–1990) from the CTRL ensemble mean and from observations CRUTEM3, remapped on a T42 grid. The annual temperature maps (°C) are shown as observed **(e)** and simulated **(f)** anomalies (ref = 1960–1990), averaged over the time period 1890–1900.

ACPD
11, 9375–9405, 2011

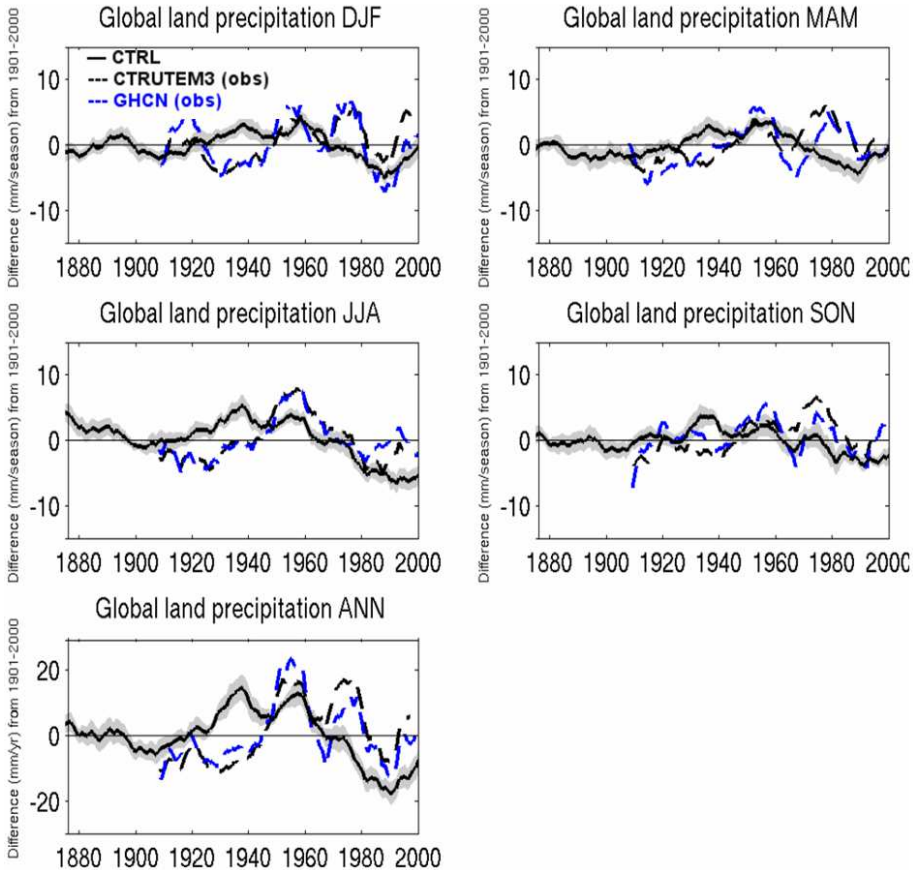

Fig. 4. Simulated (CTRL, solid) and observed (CRU, black dashed; GHCN, blue dashed) annual and seasonal global land precipitation anomalies (mm season^{-1} and mm year^{-1}, respectively), relative to the 1901–2000 mean, shown as 11-years running means. Gray shaded area corresponds to the ±1 sigma spread of the ensemble CTRL.

ACPD
11, 9375–9405, 2011

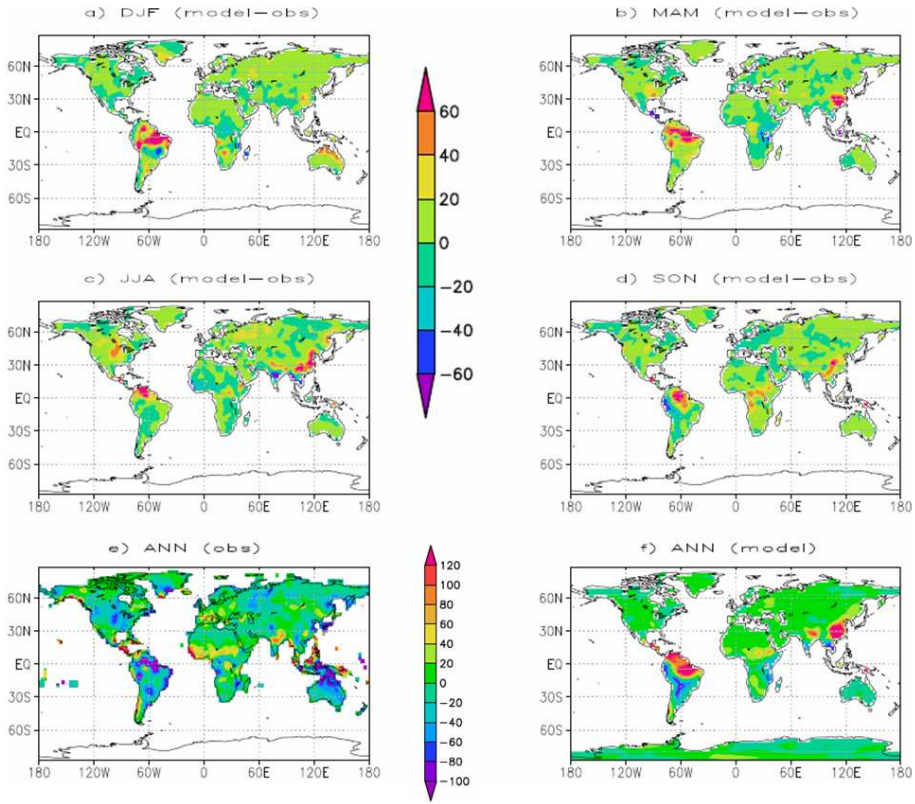

Fig. 5. Maps of seasonal land precipitation biases (mm season^{-1}), averaged over the time period 1930–1940 **(a–d)**. The biases maps correspond to the difference between the precipitation anomalies (ref = 1901–2000) from the CTRL ensemble mean and from the observations CRU. The annual land precipitation maps (mm year^{-1}) are shown as observed and simulated anomalies (ref = 1901–2000), averaged over the time period 1930–1940 **(e–f)**.

ACPD
11, 9375–9405, 2011

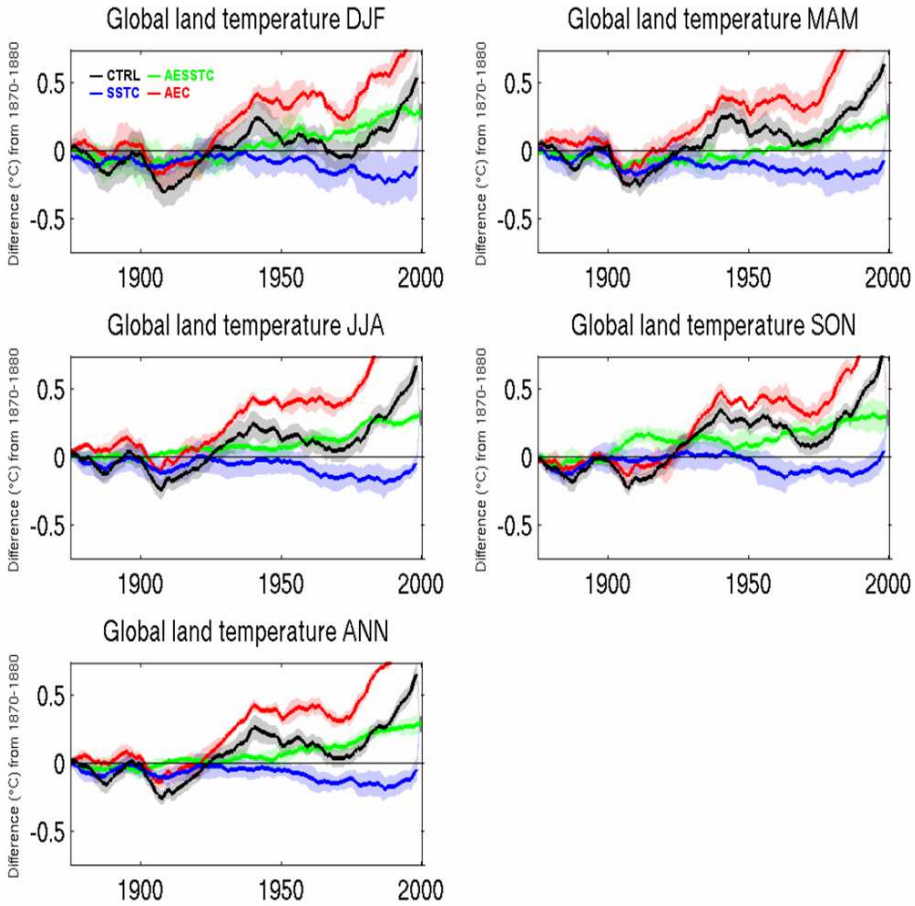

Fig. 6. Simulated annual and seasonal global land temperature anomalies (°C), relative to the 1870–1880 mean, shown as 11-years running means. Shaded areas correspond to the ±1 sigma spread of each ensemble.

ACPD
11, 9375–9405, 2011

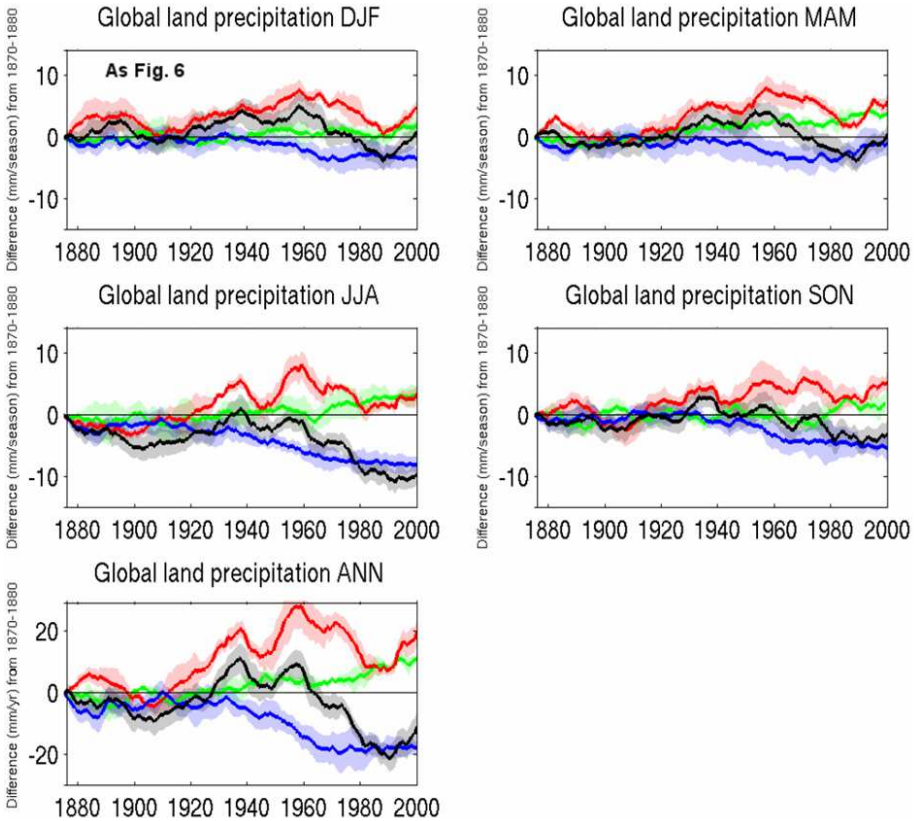

Fig. 7. Simulated annual and seasonal global land precipitation anomalies (mm season^{-1} and mm year^{-1}, respectively), relative to the 1870–1880 mean, shown as 11-years running means. Shaded areas correspond to the ±1 sigma spread of each ensemble.

ACPD
11, 9375–9405, 2011

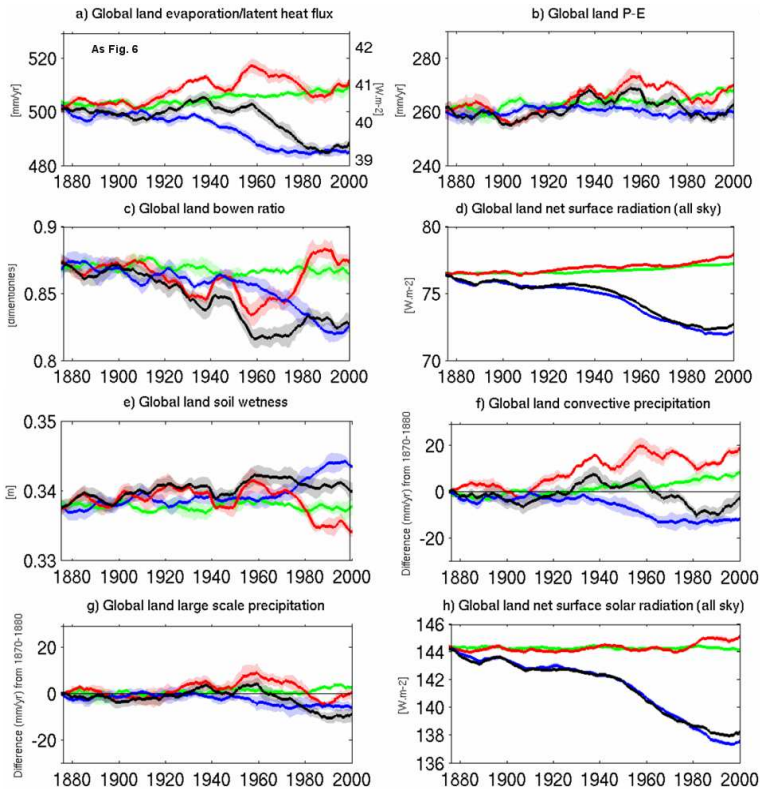

Fig. 8. Simulated annual global land mean absolute values, of evaporation (left hand side axis, mm year^{-1}) and latent heat flux (right hand side axis, W m^{-2}) **(a)**, precipitation minus evaporation (= P – E, mm year^{-1}) **(b)**, Bowen ratio **(c)**, net surface radiation all sky (W m^{-2}) **(d)**, soil wetness (m) **(e)**, net surface solar radiation all sky (W m^{-2}) **(h)**, and anomalies of convective **(f)** and large scale precipitation (mm year^{-1}) **(g)** (ref = 1870–1880), shown as 11-years running means. Shaded areas correspond to the ±1 sigma spread of each ensemble.

ACPD
11, 9375–9405, 2011

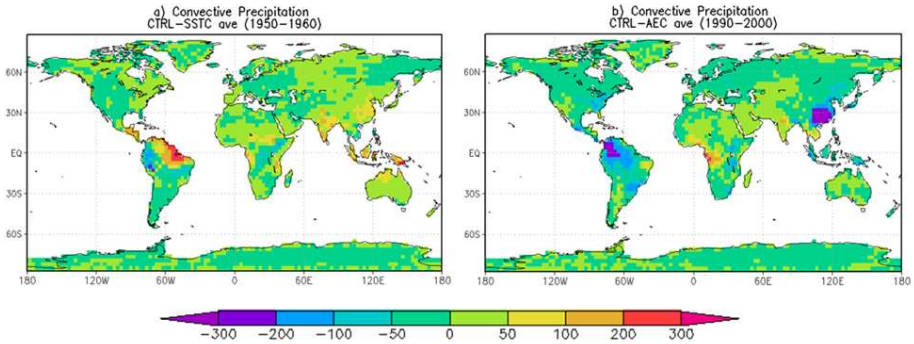

Fig. 9. Maps of annual land convective precipitation (mm year^{-1}) differences between the anomalies (ref = 1870–1880) from the CTRL and the SSTC ensemble means, averaged over the time period 1950–1960 **(a)**, and between the anomalies (ref = 1870–1880) from the CTRL and the AEC ensemble means, averaged over the time period 1990–2000 **(b)**.

ACPD
11, 9375–9405, 2011